ELECTROANALYSIS
An International Journal Devoted to Electroanalysis, Sensors and Bioelectronic Devices

Accepted Article

Title: Influence of microwave irradiation and combustion fuels on the rate capability and cycle performance of Li1.2Mn0.52Ni0.13Co0.13Al0.02O2 layered material

Authors: Funeka Nkosi, Nithyadharseni Palaniyandy, Kumar Raju, and Kenneth Ozoemena

This manuscript has been accepted after peer review and appears as an Accepted Article online prior to editing, proofing, and formal publication of the final Version of Record (VoR). This work is currently citable by using the Digital Object Identifier (DOI) given below. The VoR will be published online in Early View as soon as possible and may be different to this Accepted Article as a result of editing. Readers should obtain the VoR from the journal website shown below when it is published to ensure accuracy of information. The authors are responsible for the content of this Accepted Article.

To be cited as: *Electroanalysis* 10.1002/elan.202060373

Link to VoR: https://doi.org/10.1002/elan.202060373

WILEY-VCH

10.1002/elan.202060373

Influence of microwave irradiation and combustion fuels on the rate capability and cycle performance of $Li_{1.2}Mn_{0.52}Ni_{0.13}Co_{0.13}Al_{0.02}O_2$ layered material

Funeka Nkosi [ab]*, Nithyadharseni Palaniyandy [b], Kumar Raju [b], and Kenneth I. Ozoemena [a]

[a] Molecular Sciences Institute, School of Chemistry, University of the Witwatersrand, Private Bag 3, Johannesburg 2050, South Africa

[b] Energy Centre, Council for Scientific and Industrial Research (CSIR), Pretoria 0001, South Africa

* Corresponding author: Funeka P. Nkosi (Funeka.Nkosi@kemi.uu.se)

Accepted Manuscript

This article is protected by copyright. All rights reserved.

Graphical Abstract

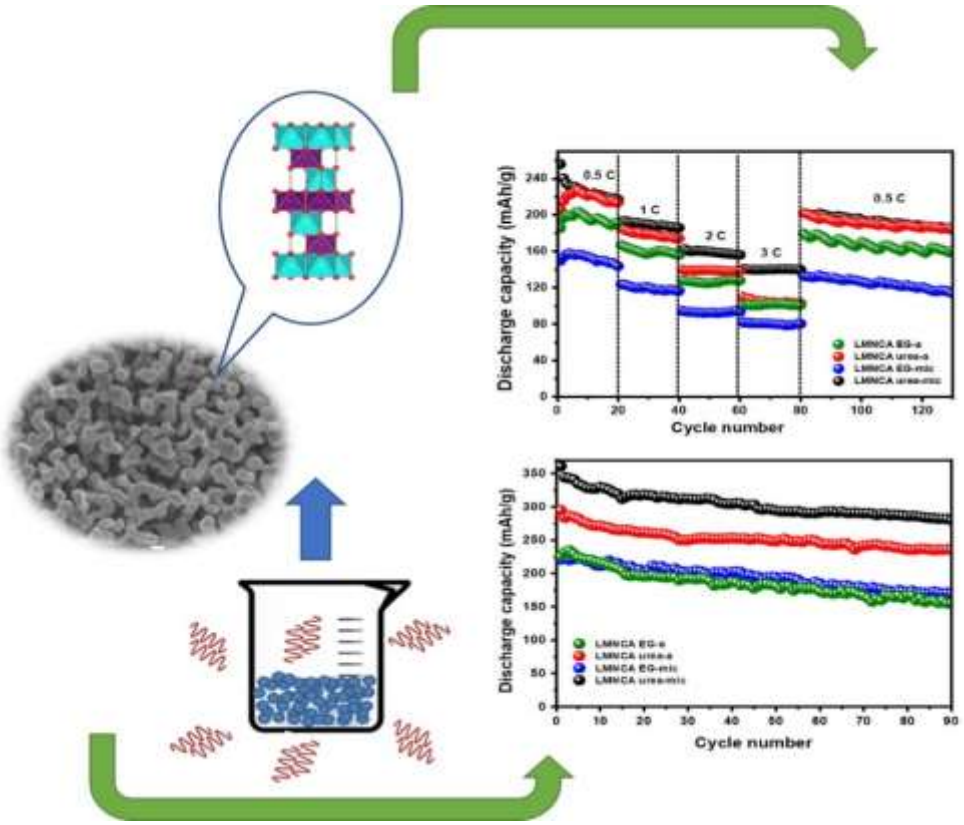

Abstract

Commercialization of lithium-manganese rich oxides (LMR-NMC) cathodes for lithium-ion batteries is hindered by shortcomings such as severe capacity fade and poor rate capability. This work reveals the synergetic effect of the structure and morphology in reducing capacity fade and improving rate capability in $Li_{1.2}Mn_{0.52}Ni_{0.13}Co_{0.13}Al_{0.02}O_2$ (LMNCA) cathode. The results show that the hybrid microwave irradiation-combustion synthesis results in smaller particles, increased lattice parameters, reduced transition metal oxidation states, and high Li-ion diffusion coefficients. These resulted in powders with reduced capacity fade and enhanced rate performance. LMNCA urea-mic exhibited the best electrochemical performance with a discharge capacity of 360 mAh/g and capacity retention of 88 % after 50 cycles at 0.1C.

Keywords: cycle performance, lithium-manganese rich oxides**,** lithium-ion batteries, rate capability, synthesis

This article is protected by copyright. All rights reserved.

Accepted Manuscript

1. Introduction

Lithium-ion batteries are reaching their energy density limit and to guarantee their application in electric vehicles in the future, high energy density (high capacity-high voltage), cheap and safe cathodes are urgently needed. Lithium-manganese-rich oxides (LMR-NMC) also denoted as $xLi_2MnO_3 \cdot (1\text{-}x)\ LiMO_2$ (M = Mn, Ni, Co) are one of the promising cathodes for future lithium-ion batteries. This is owed to their unique high reversible capacity (> 250 mAh/g), operating voltage (>3.5 V *vs.* Li^+/ Li) and energy density (> 900 Wh/kg) when charged between 2.0 – 4.8 V vs. Li^+/ Li [1–3]. LMR-NMC cathodes are also cheaper and safer compared to $LiCoO_2$ (LCO) and $Li[Ni_{1/3}Mn_{1/3}Co_{1/3}]O_2$ (NMC) cathodes because of their low cobalt content.

The structure of LMR-NMCs consists of a monoclinic Li_2MnO_3 phase with the C_2/m space group and trigonal $LiMO_2$ (M = Mn, Ni, Co) phase with the $R\bar{3}m$ space group. The compatibility of these phases allows their integration at an atomic level resulting in a layered structure with alternating transition metal layers and lithium layers [1,4–6]. The resultant layered structure provides a two-dimensional pathway for lithium-ion conduction (Figure S1). LMR-NMC cathodes exhibit unexpected high specific capacities beyond their theoretical capacity because of capacity contributions from both the transition metal cation redox in the $LiMO_2$ and Li_2MnO_3 activation when the cathodes are initially cycled [7]. Initial charging of LMR-NMC to 4.4 V *vs.* Li^+/Li results in lithium-ions extracted from the LMO_2 with concomitant oxidation of Ni^{2+} to Ni^{4+} and Co^{3+} to Co^{4+}. More lithium-ions are extracted from further charging above 4.4 V *vs.* Li^+/Li, which results in lithium extraction with concomitant oxidation O^{2-} anions from the Li_2MnO_3 phase [8– 11]

However, severe capacity fade and poor rate capability are amongst the main problems halting the commercialization LMR-NMC cathodes[12–15]. Poor rate capability is due to the low lithium-ion diffusion coefficient in Li_2MnO_3 and low electronic conductivity because of the existence of Mn^{4+}ions [1,7,16–18]. Capacity fade is caused by the spinel formation occurring during cycling and poor morphology of the cathode powders. Spinel formation occurs in $LiMO_2$ due to cation mixing [19–21], while in the Li_2MnO_3 is caused by the removal of Li^+ and O^{2-} during the Li_2MnO_3 activation [20]. The spinel formation then causes capacity fade by blocking the Li-ion diffusion channels [20].

Different strategies including doping [22–24], coating [25,26], and employing different synthesis methods [27,28] have been explored in improving the electrochemical performance

This article is protected by copyright. All rights reserved.

Accepted Manuscript

of LMR-NMC. Out of these strategies, synthesis is the most effective strategy because the capacity fade and rate-capability in LMR-NMC are closely related to the structure, stoichiometry, and morphology which could be simultaneously controlled by the synthesis methods and conditions[27].

Combustion synthesis is one of the fast, cheap, and effective synthesis methods for preparing various cathodes for lithium-ion batteries. Urea and ethylene glycol (EG) fuels are examples of two types of fuels widely used for the combustion synthesis. Urea is a form of a nitrogen-based fuel resulting in a rapid and high energy combustion reaction, while EG is a form of carbohydrate-based fuel resulting in a controllable and stable combustion reaction. Their different gel stabilities and flame temperature properties result in powders with different morphologies and particle sizes [29,30]. The dielectric heating offered by microwave irradiation has been shown to be beneficial for tuning oxidation states of metal ions in cathodes for batteries [31–34].Therefore, the hybrid microwave irradiation-combustion synthesis could allow the improvement of rate-capability and capacity retention in LMR-NMCs by controlling particle size and morphology using different combustion fuels, and controlling the structure and oxidation states of the transition metals using microwave irradiation.

Herein, the hybrid microwave irradiation-combustion synthesis was used to prepare LMNCA cathodes *viz*. LMNCA urea-a, LMNCA EG-a, LMNCA urea-mic, and LMNCA EG-mic. The average particle size was 79.5, 95.1, 60.0 and 57.1 nm, for LMNCA urea-a, LMNCA EG-a, LMNCA urea-mic, and LMNCA EG-mic, respectively. The discharge capacity at 0.1 C was 295, 240, 360, and 221 mAh/g for LMNCA urea-a, LMNCA EG-a, LMNCA urea-mic, and LMNCA-EG mic, respectively. The order of increased capacity retention and rate capability was LMNCA-urea-mic > LMNCA EG-mic> LMNCA urea-a > LMNCA EG-a. This work also revealed the synergetic effect of structure, transition metal oxidation states and morphology in reducing capacity fade and improving rate capability in LMR-NMC cathodes which is often overlooked for such cathodes.

Accepted Manuscript

This article is protected by copyright. All rights reserved.

2. Experimental

2.1 Sample preparation

Stoichiometric amounts of $LiNO_3$ (Sigma Aldrich) with 10 % excess lithium, Mn $(NO_3)_2 \cdot 4H_2O$ (Sigma Aldrich), Ni $(NO_3)_2 \cdot 6H_2O$ (Sigma Aldrich), Co $(NO_3)_2 \cdot 6H_2O$ (Associated Chemical Enterprises (ACE), Al $(NO_3)_3 \cdot 9H_2O$ (Fluka Analytical) and urea ($(CO(NH_2)_2$), Merk) fuel were dissolved completely in de-ionized water. The mixture was stirred for 1 h using a magnetic stirrer at room temperature. The resultant solution was transferred into a crucible and combusted in at 500 ºC for 10 min using a muffle furnace (MTI, KSL-1700X-S-UL). The resultant powders were allowed to cool to room temperature. The powders were then ground into a fine powder and were subjected to microwave irradiation (Anton Paar Multiwave 3000 system, $\lambda = 0.12236$ m) at 600 W for 20 min before annealing at 800 ºC for 9 h in air. The obtained powders were named LMNCA urea-mic, and LMNCA urea-a powders were obtained when the procedure was followed without the microwave irradiation step. Similar synthesis procedure was used for the EG combustion synthesis where EG $(CH_2OH)_2$ (Sigma Aldrich) fuel was used and the resultant powders were named LMNCA EG-mic. LMNCA EG-a powders were obtained using the similar procedure but without the microwave irradiation step. The schematic representation of the preparation of the LMNCA powders is shown in Figure 1.

Accepted Manuscript

This article is protected by copyright. All rights reserved.

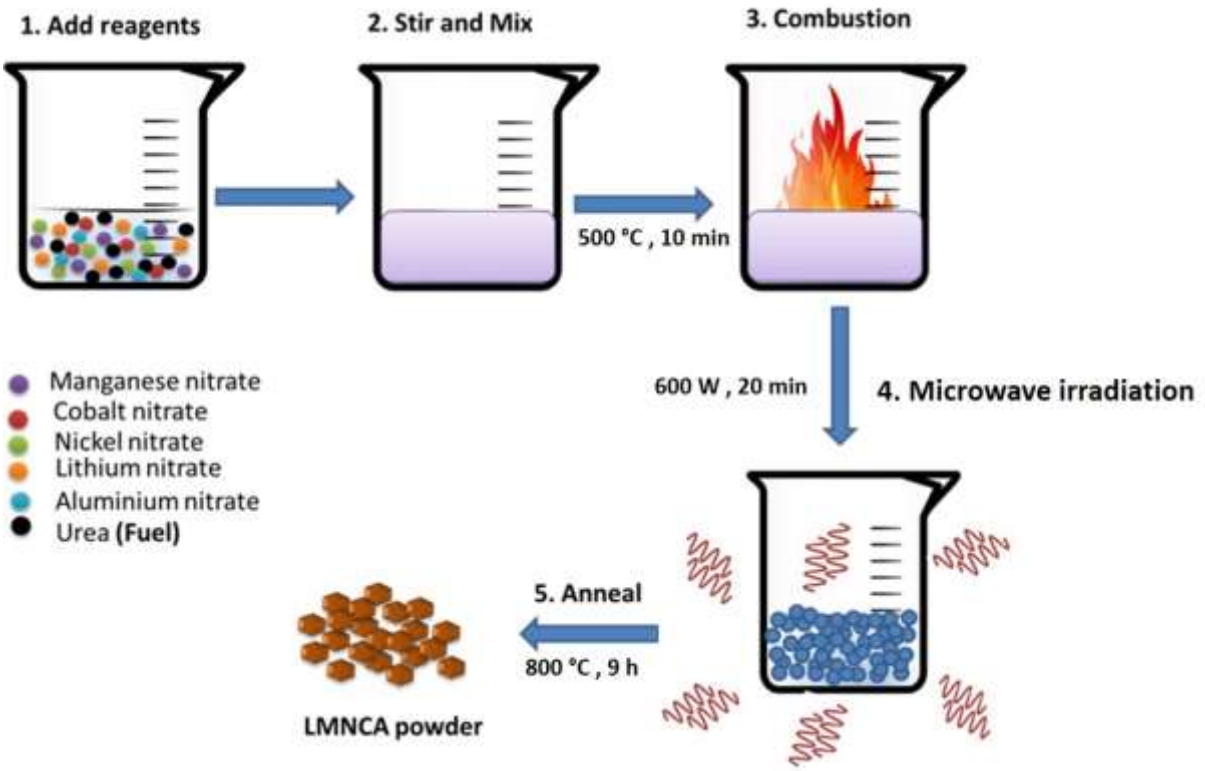

Figure 1: Hybrid microwave irradiation-combustion synthesis of LMNCA powders.

2.2Materials Characterization

2.2.1 Structural and physical measurements

Powder X-ray analysis was carried out on a PANalytical X'Pert Pro diffractometer with CuKα radiation (λ=1.5046 Å, 45 kV, 40 mA,). The XRD diffractograms were obtained in a scan range between 0 and 90°. The lattice parameters and crystal information were obtained by Rietveld refinement using a Topas software. The Raman spectra were acquired using a Horiba LabRAM HR Raman spectrometer with an Olympus BX41 microscope attachment. The excitation wavelength was the 514.5 nm line and the beam power at the sample was 0.4 mW. Raman spectra were measured up to 1000 cm^{-1} on the stokes side, with a spectral resolution of about 3 cm^{-1}. Scanning electron microscopy (SEM) was to determine the morphology of the samples. The prepared samples were examined using the field emission scanning electron microscope (FE-SEM) (JSM-7500F, JEOL) with the acceleration voltage of 2.00 kV. The samples were coated with carbon during sample preparation to prevent charging. A SEM/EDX combined equipment was used for the EDX analysis of the samples.

This article is protected by copyright. All rights reserved.

Accepted Manuscript

X-ray photoelectron spectroscopy (XPS) measurements were carried out using the Thermo ESCA lab 250Xi with monochromatic Al Kα radiation (1486.7 eV). X-ray power of 300 W and X-ray spot size 900 μm was used. The binding energy was calibrated with reference to the C 1s level of the carbon (284.6 eV). The average oxidation state of manganese ions (V_{Mn}) in the samples was calculated from the following linear equation between V_{Mn} and ΔE_{3s}.

$$V_{Mn} = 7.875 - 0.893\Delta E_{3s} \quad (1)$$

Where V_{Mn} is the average oxidation state of manganese ions and $\Delta E_{3s}$is the energy separation between the Mn 3s peaks.

2.3Electrochemical measurements

2.3.1 Cell fabrication

The cathodes were prepared by the making up of slurry containing 80 % active material (prepared sample), 10 % carbon black and 10 % polyvinylidene fluoride (PVDF) binder in N-methyl-2-pyrrolidone (NMP) solvent. The slurry was coated onto an aluminium current collector using a doctor-blade method. The coated aluminium foil was then dried under vacuum at 110 ^{o}C for 12 h, before being pressed to form a uniform layer and cut into circular disk electrodes. The electrodes were dried at 110 ^{o}C overnight for battery fabrication. The electrochemical performance of the prepared materials was evaluated using a two-electrode coin-type cell. The coin cells consist of the prepared electrodes as cathode, lithium foil as an anode and the electrolyte (1 M $LiPF_6$ in EC/DEC/DMC in 1:1:1). The cells were fabricated in an Ar- filled glove box with ultra (MBRAUN MB10) compact. The coin cells were allowed to stand for 24 h before performing the electrochemical measurements.

2.3.2 Electrochemical characterisation

Cyclic voltammetry (CV) measurements were carried out using a Bio-Logic VMP3-based instrument. CV scans were recorded at a scan rate of 0.1 mV s^{-1} between 2.0 and 4.8 V (vs. Li^+/Li). Galvanostatic charge-discharge measurements were carried using a Maccor 4000 battery tester. The charge-discharge measurements were recorded at 0.1 C between 2.0 and 4.8 V (vs. Li^+/Li). The rate capability of the materials was performed at different C-rates (charge-discharge rates). Electrochemical impedance spectroscopy (EIS) studies were carried out using a Bio-Logic Science VMP3-based instrument. The EIS measurements were performed in the range from 100 kHz to 10 mHz with an AC signal amplitude of 10 mV. The data acquisition

Accepted Manuscript

This article is protected by copyright. All rights reserved.

and analysis were done using the EC-lab V10.32 software. The diffusion coefficient of lithium ions in the cathodes was calculated using the Warburg parameter obtained from the EIS data. The following equation was used [95]:

$$D_{Li} = \frac{2R^2\ T^2}{n^4\ F^4\ \sigma^2 A^2\ C_{Li}^2} \quad (2)$$

where D_{Li} is the lithium ion diffusion coefficient, R is the gas constant, T is the absolute temperature, n is the number of electrons transferred, F is the Faraday constant, σ is the Warburg parameter, A is the geometric surface area of the cathode and C_{Li} is the concentration of lithium in the cathode material. The Warburg factor (σ) is obtained from the slope of a plot of real impedance (Z') vs. reciprocal square root of frequency ($\omega^{-1/2}$) in the low frequency region. The following equation is then used for the plot:

$$Z = \sigma\ (1 - j)\omega^{-1/2} \quad (3)$$

Accepted Manuscript

This article is protected by copyright. All rights reserved.

3. Results and discussions

3.1 Morphology and Structure characterization

Figure 2 shows the SEM images of the samples. LMNCA urea-a and LMNCA EG-a exhibit particles with an average diameter range of 60-110 nm (79.5 nm) and 80-200 (95.1 nm) nm, respectively. LMNCA urea-a and LMNCA EG-a samples have different morphology and particle sizes due to different flame properties and gas evolution processes effected by urea and EG fuels. However, both LMNCA urea-mic and LMNCA EG-mic exhibit smaller particle sizes with narrow distribution, the particle sizes were 50-90 nm (60 nm) and 50-100 nm (57.1 nm), respectively. The EDX spectra shown in Figure S2 confirmed the elements present in the samples.

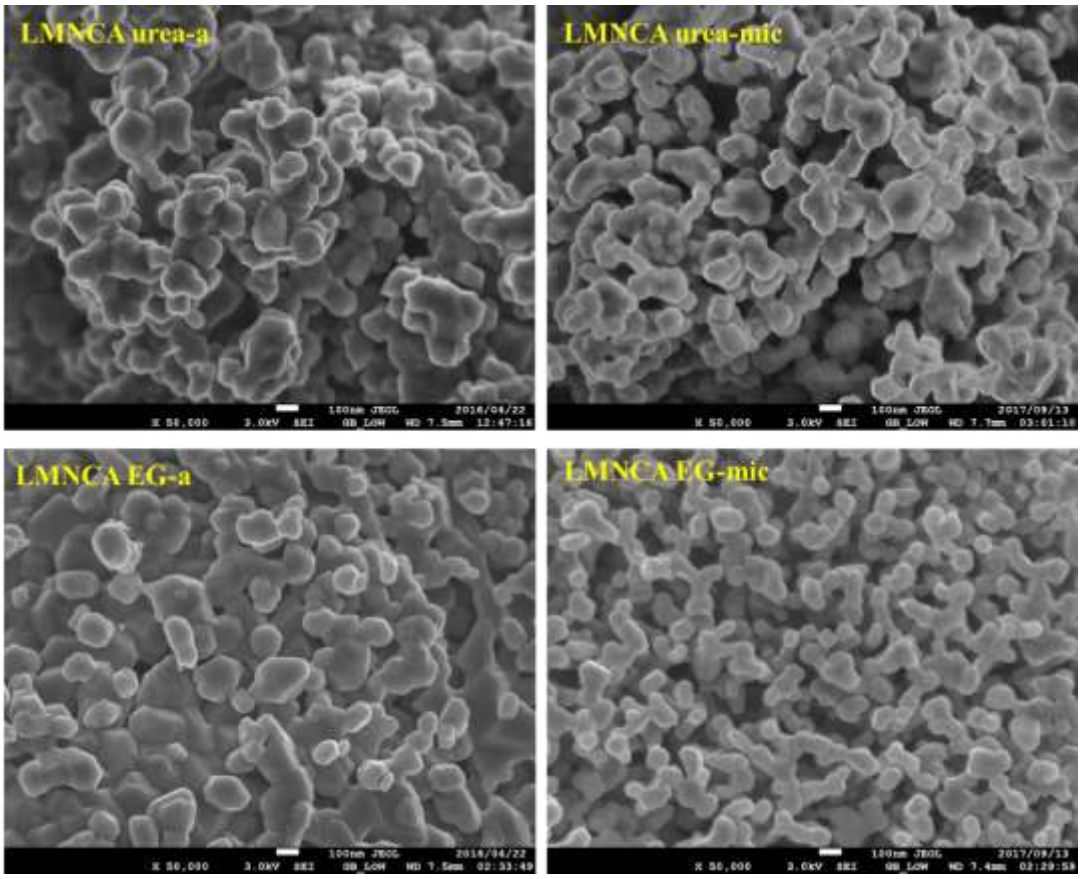

Figure 2: SEM images of LMNCA urea-a, LMNCA EG-a, LMNCA urea-mic and LMNCA EG-mic samples.

This article is protected by copyright. All rights reserved.

Accepted Manuscript

Figure 3a shows the PXRD patterns of the LMNCA-urea-a, LMNCA-EG-a, LMNCA-urea-mic and LMNCA-EG-mic samples. The relatively strong peaks were indexed to the $LiMO_2$ phase based on the hexagonal structure with the space group $R\bar{3}m$ (PDF# 00-056-0147). While the peak between 20-25º was indexed to Li_2MnO_3 phase based on the monoclinic structure with the space group (C_2/m) (PDF# 04-011-3411). The PXRD patterns are without impurity peaks revealing that the microwave irradiation did not cause the decomposition of the samples and formation of other phases.

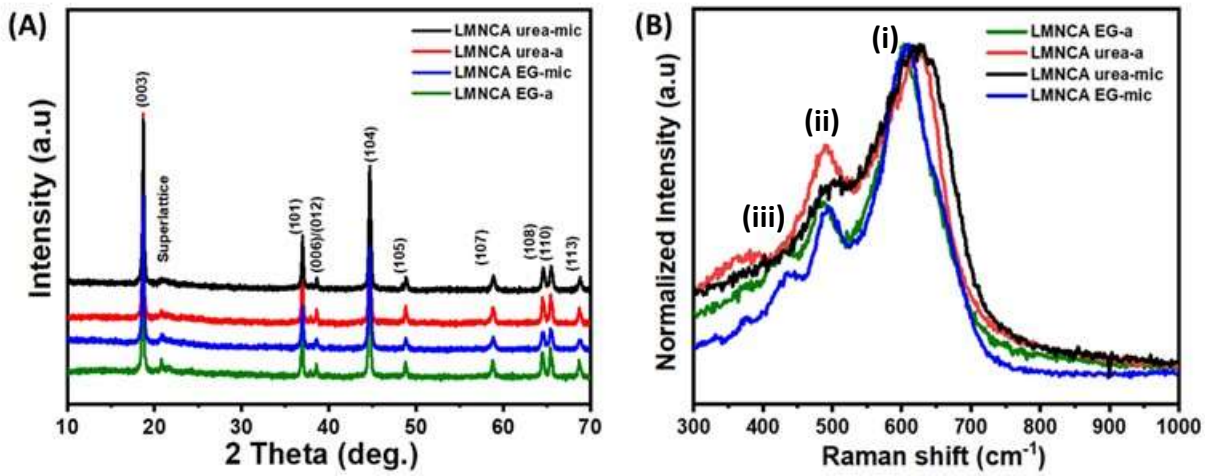

Figure 3: (a) XRD patterns and (b) Raman spectra of LMNCA urea-a, LMNCA EG-a, LMNCA urea-mic and LMNCA EG-mic samples.

The lattice parameters *a* and *c* were calculated using Rietveld refinement using the $R\bar{3}m$ space group. The calculated lattice parameters with other structural parameters are summarized in Table 1. The obtained lattice parameters are consistent with the values reported in literature[35,36]. The lattice parameter *a* represent the metal to metal distance in the transition metal layer and lattice parameter *c* is the inter-slab distance. The clear splitting of the (108)/(110) doublet peaks and the axis ratio *c/a* close to 5 for all the samples indicates good hexagonal ordering [35]. LMNCA-urea-mic and LMNCA-EG-mic samples have slightly increased lattice parameters compared to LMNCA-urea-a and LMNCA-EG-a. The increase in lattice parameters is due to the reduction expansion mainly caused by reduction of transition metal cation oxidation states and the corresponding increased cation radii of the reduced transition metals cations [37,38]. The slight increase in the lattice parameters and unit cell

This article is protected by copyright. All rights reserved.

Accepted Manuscript

volume for microwave irradiation LMNCA urea-mic and LMNCA EG-mic suggests better lithium diffusion in the structure. The small lattice contraction that maybe caused by oxygen vacancies has minor effect in the lattice parameters for nonstoichiometric compounds [37,39,40]. The $I_{(003)}/I_{(104)}$ intensity ratio is usually used to characterized the degree of cation mixing in the Li layer formed by some Ni^{2+} ions occupying Li^{+} sites due to similar radii of Li^{+} (0.76 Å) and Ni^{2+} (0.69Å) [41–43]. $I_{(003)}/I_{(104)}$ intensity ratio is 1.26, 1.33, 1.37 and 1.47 for LMNCA urea-a, LMNCA EG-a, LMNCA urea-mic and LMNCA EG-mic, respectively. Higher $I_{(003)}/I_{(104)}$ intensity ratio obtained for microwaved samples indicates lower degree of cation mixing beneficial for improving the cycle performance.

Table 1: Summary of fitted crystallographic parameters

Materials	**Lattice parameter ±0.003 (Å)**	**Axis ratio *(c/a)***	**$I_{(003)}/I_{(104)}$ ratio**	**Cell volume ±0.002 (Å^3)**	**R_p (%)**	**R_{wp} (%)**	**R_{bragg} (%)**
LMNCA-EG	***a***-2.851 ***c***-14.240	4.995	1.33	100.27	1.91	2.47	1.323
LMNCA-urea	***a***-2.850 ***c***-14.229	4.993	1.26	100.00	1.97	2.58	1.529
LMNCA-EG-mic	***a***-2.853 ***c***-14.249	4.994	1.47	100.44	2.02	2.63	1.336
LMNCA-urea-mic	***a***-2.852 ***c***-14.239	4.993	1.37	100.30	1.89	2.45	1.478

Furthermore, Figure 3b shows the Raman spectra of LMNCA urea-a, LMNCA EG-a, LMNCA urea-mic and LMNCA EG-mic samples to investigate the local structure of the samples. The Raman spectra show three Raman active bands around (i) 605 (ii) 497 and (iii) 431 cm^{-1}. The peaks around 605 and 497 $cm^{-1}$are attributed to the A_{1g} mode of the M-O stretch, E_g mode of the O-M-O bend in $LiMO_2$, respectively [44]. The peak at 431 cm^{-1} is attributed to the A_g and B_g modes in the Li_2MnO_3 [44]. The results confirm the existence of the two phases observed in the XRD analysis. The Raman spectra show a slight change of peaks at (ii) and (iii) for LMNCA

This article is protected by copyright. All rights reserved.

Accepted Manuscript

urea-mic and LMNCA EG-mic compared to LMNCA urea-a and LMNCA EG-a, possibly suggesting a slight change in $LiMO_2$ and Li_2MnO_3 local environments.

Figure 4 shows that the Co $2p_{3/2}$, Ni $2p_{3/2}$, Mn $2p_{3/2}$ and O 1s X-ray photoelectron spectroscopy (XPS) analyses of the samples. Table 2 show the XPS fitted data for all the samples. Figure 4a shows the Co $2p_{3/2}$ spectra of the samples with the binding energies around 780 eV. The full-width at half-maximum (FWHM) about 1.8 eV and the energy separation value between the the Co $2p_{3/2}$ and Co $2p_{1/2}$ peaks of ca.15 eV (Figure S3) indicating that the Co ions are in the +3-oxidation state for all the samples [45]. Figure 4b shows the Ni $2p_{3/2}$ spectra of the samples, the broadness of the Ni $2p_{3/2}$ peak with FWHM *ca.* 3 eV indicates the existence of Ni^{2+} and Ni^{3+}ions and the fitted data of the Ni $2p_{3/2}$ peak exhibited in Table 2. There is slight increase of the Ni^{2+}ions by microwave irradiation. Mn 2p and Mn 3s spectra shown in Figure S2 were used to confirm the average manganese oxidation state since the manganese ions are present in the +4-oxidation state in Li_2MnO_3 and +3-oxidation state in $LiMO_2$ phases. The binding energy separation of the Mn 3s peaks (ΔE_Mn3s) and Mn 2p peaks (ΔE_Mn2p) is between 4.3 - 4.7 eV and 11.5 eV, respectively, revealing that most of the Mn ions in are +4-oxidation state. Figure 4c shows the Mn $2p_{3/2}$ peak with FWHM *ca.* 3 eV also indicating existence of Mn^{3+}ions. The fitted data of the Mn $2p_{3/2}$ peak exhibited in Table 2 shows that similar Mn^{3+}/Mn^{4+} ratio and average Mn oxidation state was obtained for both LMNCA urea-a and LMNC EG-a. However, the microwaved samples LMNCA urea-mic and LMNC EG-mic exhibited reduction of Mn^{4+} ions. The Mn^{4+} ions content is 78, 78, 72 and 59 % for LMNCA urea-a, LMNCA EG-a, LMNCA urea-mic and LMNCA EG-mic, respectively. Figure 4d shows the O 1s spectra of the samples. The main peak at 530.1 eV corresponds to the lattice oxygen, whereas the higher binding energy peaks at 531.8 and 533.9 eV correspond to OH^- and H_2O species, respectively[46]. The peak at 531.8 eV also corresponds to the oxygen vacancies in metal oxides [47–49]. The fitted data for O 1s peak is shown in Table 2, the LMNCA-EG-mic and LMNCA-urea-mic show low lattice oxygen content and high content of the surface hydroxyl oxygen compared to the non-microwaved samples. These changes both suggest the formation of more oxygen vacancies by microwave irradiation. The formation of oxygen vacancies is due to the entropy-driven desorption of lattice oxygen induced by microwave irradiation and the balancing of charges in the lattice as a consequence of the reduction of oxidation states of transition metal ions.

This article is protected by copyright. All rights reserved.

Accepted Manuscript

10.1002/elan.202060373

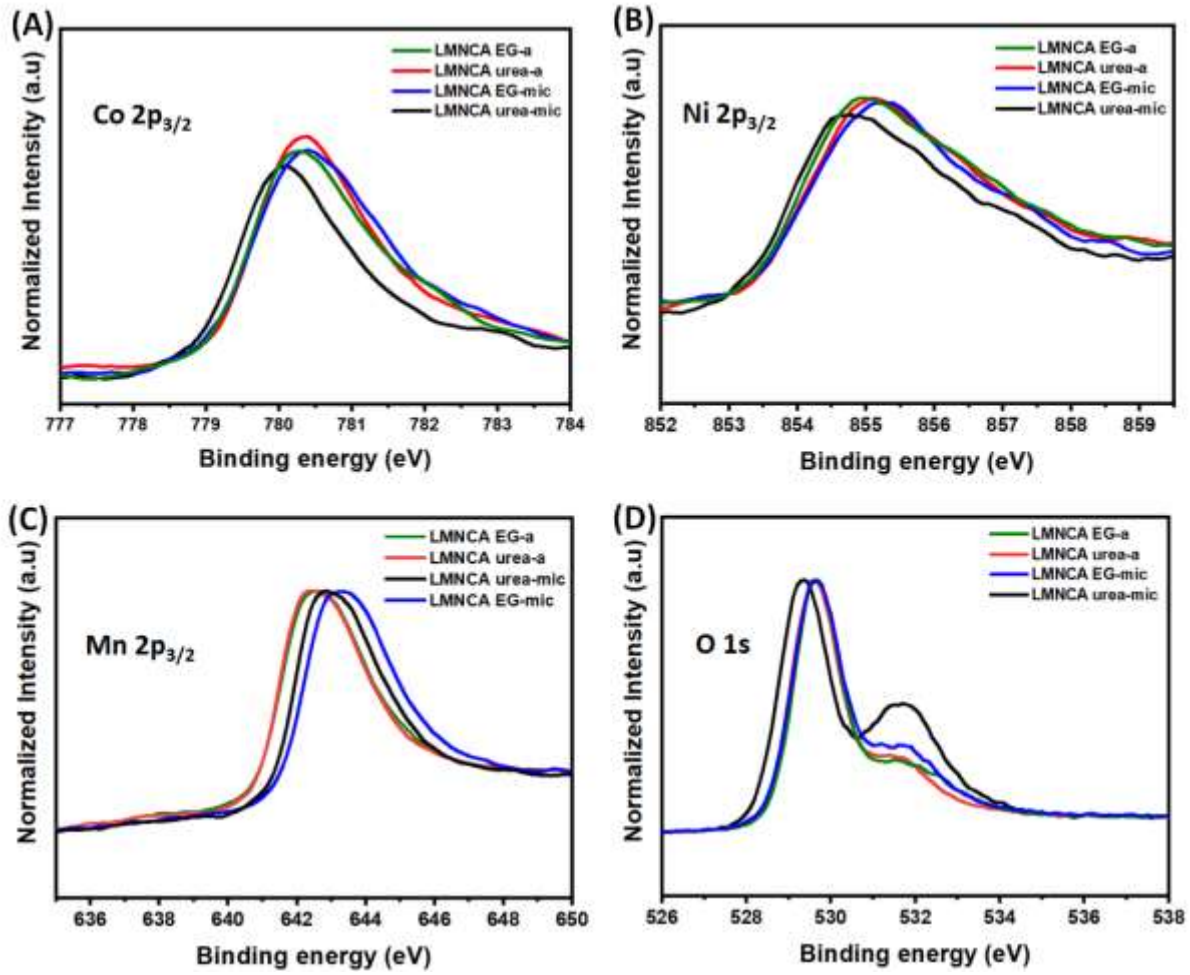

Figure 4: XPS data of (a) Co $2p_{3/2}$, (b)Ni $2p_{3/2}$, (c) Mn $2p_{3/2}$ and (d) O 1s for of LMNCA urea-a, LMNCA EG-a, LMNCA urea-mic and LMNCA EG-mic samples.

Accepted Manuscript

This article is protected by copyright. All rights reserved.

Table 2: Summary of the fitted XPS data for LMNCA urea-a, LMNCA EG-a, LMNCA urea-mic and LMNCA EG-mic samples

Sample	Ni^{3+}	Ni^{2+}	Mn^{4+} (%)	Mn^{3+} (%)	Mn^{3+}/Mn^{4+}	O_{latt}	O_v	O_{ads}	Average oxidation state of Mn
LMNCA EG-a	53	47	77	23	0.29	54	34	12	3.95
LMNCA urea-a	42	58	79	21	0.26	61	22	17	3.95
LMNCA EG-mic	40	60	59	41	0.70	57	43	1	3.68
LMNCA urea-mic	41	59	72	28	0.39	52	44	4	3.77

Accepted Manuscript

This article is protected by copyright. All rights reserved.

3.2 Electrochemical performance studies

Figure 5a shows the cyclic voltammograms of LMNCA materials recorded at a scan rate of 0.1 mV s^{-1} in the voltage range of 2.0 – 4.8 V *vs.* Li/Li^+. The broad peak at about 4.2 V corresponds to the oxidation of both the Ni^{2+} to Ni^{4+} and Co^{3+} to Co^{4+} in the structure since they occur at similar oxidation potential[50]. The Mn^{3+}/ Mn^{4+} redox is inactive during the initial cycle until the activation of the Li_2MnO_3 phase. The peak at ~4.7 V corresponds to the activation of the Li_2MnO_3 phase. The reduction peaks between 3.7 and 4.5 V corresponds to the reduction of Ni^{4+} to Ni^{2+} and Co^{4+} to Co^{3+} due to the lithium deintercalation in the tetrahedral and octahedral sites, respectively [50]. The reduction peak at ~3.2 V is due to the reduction of Mn^{4+} in the spinel-like MnO_2 phase formed by Li_2MnO_3 activation. The reduced Li_2MnO_3 activation in the LMNCA urea-a and LMNCA EG-a compared to the LMNCA EG-mic and LMNCA urea-mic is indicated by the reduced peak intensity ratio between the peaks at *ca.* 4.2 V and 4.5 V. The actual contributions of the transition metal redox processes to the electrochemical performance are shown in Figure 6.

Figure 5b displays the galvanostatic charge-discharge between 2.0 - 4.8 V at 0.1 C *(vs.* Li/Li^+). Similar to the cyclic voltammograms, the first voltage plateau around 4.1 V is attributed to the de-lithiation of the $LiMO_2$ (M = Mn, Ni, Co) phase corresponding to the oxidation of the Ni^{2+} to Ni^{4+} and Co^{3+} to Co^{4+} and the second voltage plateau above 4.4 V is due to the activation of the Li_2MnO_3 phase. The discharge capacity was 295, 240, 360 and 221 mAh/g for LMNCA urea-a, LMNCA EG-a, LMNCA urea-mic and LMNCA EG-mic, respectively. Figure 5c shows the cycle performance of the samples cycled at 0.1 C between 2.0 - 4.8 V *(vs.* Li/Li^+). The capacity retention at 0.1 C after 50 cycles was 84, 78, 88, and 82 % for LMNCA urea-a, LMNCA EG-a, LMNCA urea-mic and LMNCA EG-mic, respectively. Figure 5d shows the cycle performance of LMNCA urea-mic and LMNCA EG-mic at 2 C to further demonstrate the enhanced cycle performance for LMNCA urea-mic and LMNCA EG-mic at high current rates. The improved cyclic performance especially for the LMNCA urea-mic and LMNCA EG-mic is due to smaller particle sizes and enhanced structure i.e larger lattice parameter and lower degree of cation mixing. The coulombic efficiency (CE) is above 90 % after 6 cycles for all samples. Figure 5e shows the rate capability performance at different current rates at 0.5, 1, 2, and 5 C over 20 cycles at each current rate. The rate capability increased for LMNCA-urea-mic > LMNCA EG-mic> LMNCA urea-a > LMNCA EG-a. The improved in rate capability in LMNCA urea-mic and LMNCA EG-mic samples is mainly due to the reduced particle sizes and enhanced electronic conductivity due to formation of more oxygen vacancies and reduction

This article is protected by copyright. All rights reserved.

Accepted Manuscript

of Mn^{4+} ions content. Smaller particle sizes with high surface area decrease the diffusion length for Li-ion transportation and the creation of surface oxygen vacancies facilitates the charge transfer at the electrode or particle surface, thus improving the rate capability.

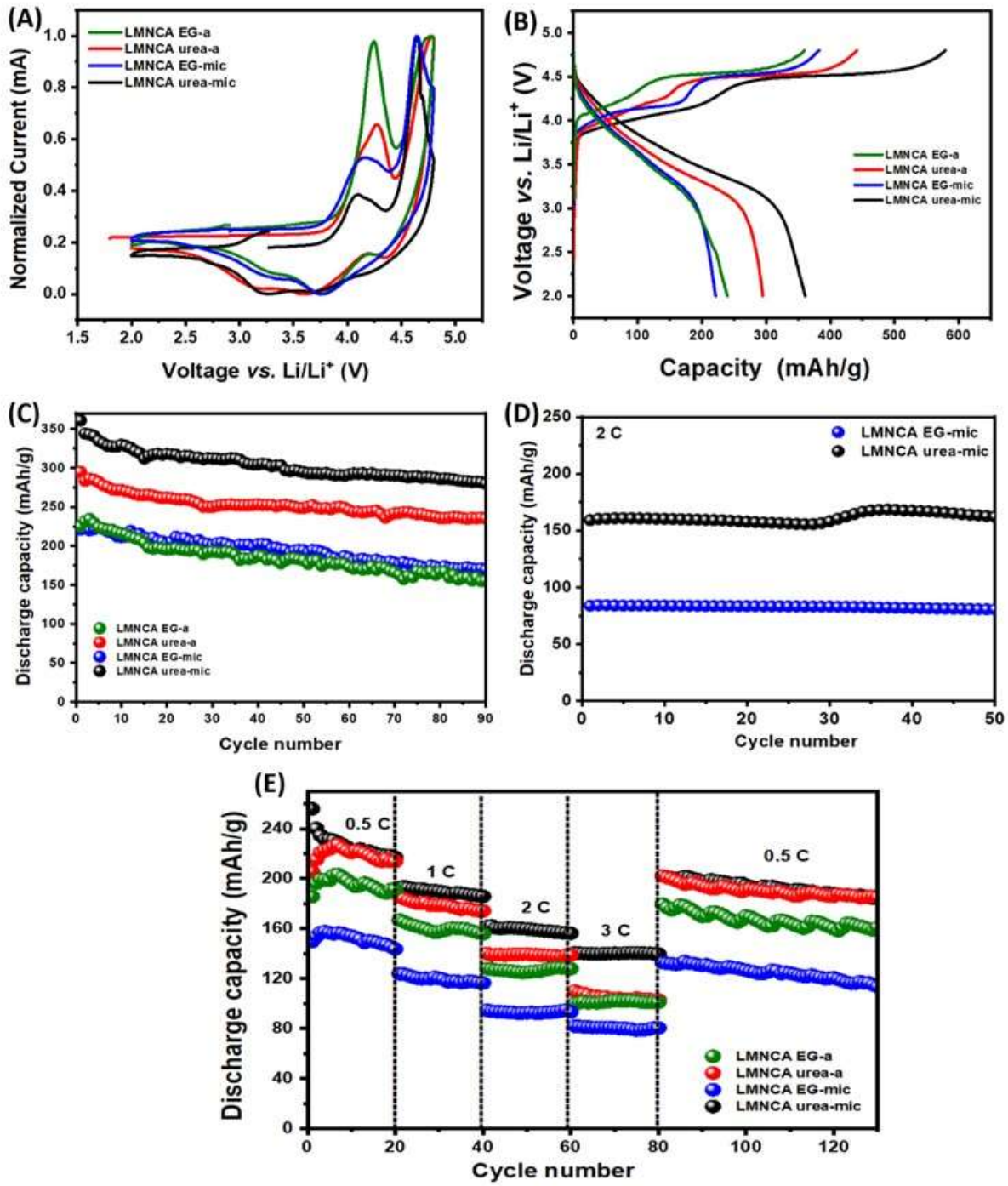

Figure 5: (a) Cyclic voltammetry at 0.1 mV s^{-1} (b) Galvanostatic charge-discharge 1st cycles at 0.1 C (c) Cycle performance at 0.1 C measured (d) Cycle performance at 2C, and (e) Rate

This article is protected by copyright. All rights reserved.

Accepted Manuscript

capability at 0.5, 1, 2, and 5 C for LMNCA urea-a, LMNCA EG-a, LMNCA urea-mic and LMNCA EG-mic samples. All studies were measured between 2.0 – 4.8 V vs. Li/Li^+.

Figure 6(c-d) shows the differential capacity curves (dQ/dV *vs.* V) of the samples after the 1^{st}, 2^{nd}, 10^{th}, 30^{th}, 50^{th} and 90^{th} charge-discharge cycles. The dQ/dV redox couples around 3.7- 4.2 V correspond to the reversible Ni^{2+} to Ni^{3+} to Ni^{4+} and Co^{3+} to Co^{4+} redox processes. High oxidation of the peak around 3.7- 4.2 V for LMNCA urea-mic and LMNCA EG-mic compared to the LMNCA urea-a and LMNCA EG-a corresponds to the increase in Ni oxidation as a consequence of the higher Ni^{2+} content exhibited by LMNCA urea-mic and LMNCA EG-mic. The intense oxidation peak around 4.5 V is due to the activation of Li_2MnO_3 phase and gives no corresponding reduction peaks since this process is irreversible. The activation process induces a new Mn^{4+}/Mn^{3+} reduction peak at ~3.3 V. This peak shifts to lower voltages upon cycling and a new peak at about 2.8 V appears due to the growth of a new spinel phase. The corresponding oxidation peak of Mn^{3+}/Mn^{4+} couple is at 3.0 - 3.2 V. The intensity of this new Mn^{4+}/Mn^{3+} reduction peak slightly changes upon cycling and is same during 1^{st} cycle and 90^{th}, suggesting limited effect of the spinel phase in the cycle performance. Figure S4 shows the post-mortem XRD analysis of LMNCA urea-a and LMNCA EG-a samples after 100 cycles at 0.1 C. The XRD results show that the materials still display a layered structure. However, the superlattice peaks between 2 Theta = 20-22° disappeared, confirming the activation of the Li_2MnO_3 phase upon cycling. Though the spinel formation was confirmed by the differential capacity curves (dQ/dV *vs.* V), the XRD analysis could not detect the spinel phase and this may be that only small amounts of the spinel phase is formed. This also expected for LMNCA urea-mic and LMNCA EG-mic.

The Mn^{3+}/Mn^{4+} oxidation for the LMNCA EG-a and LMNCA EG-mic samples is suppressed indicating that the Mn^{3+}/Mn^{4+} redox have limited contribution to the capacity. Tarascon et. al. also reported that the peak at 3.3 V has a contribution from O^{2-}/O^{n-}anion redox which is also responsible for additional capacity in LMR-NMC cathodes [7]. The peak potential difference between the 1^{st} and 90^{th} cycles for the peak at 3.3 V was also smaller for the EG-based samples *viz.* 560, 490, 570 and 530 mV for LMNCA-urea, LMNCA-EG, LMNCA-urea mic and LMNCA-EG mic, respectively. Therefore, these observations explain the lower capacities obtained for EG-based samples compared to the Urea-based samples.

This article is protected by copyright. All rights reserved.

Accepted Manuscript

10.1002/elan.202060373

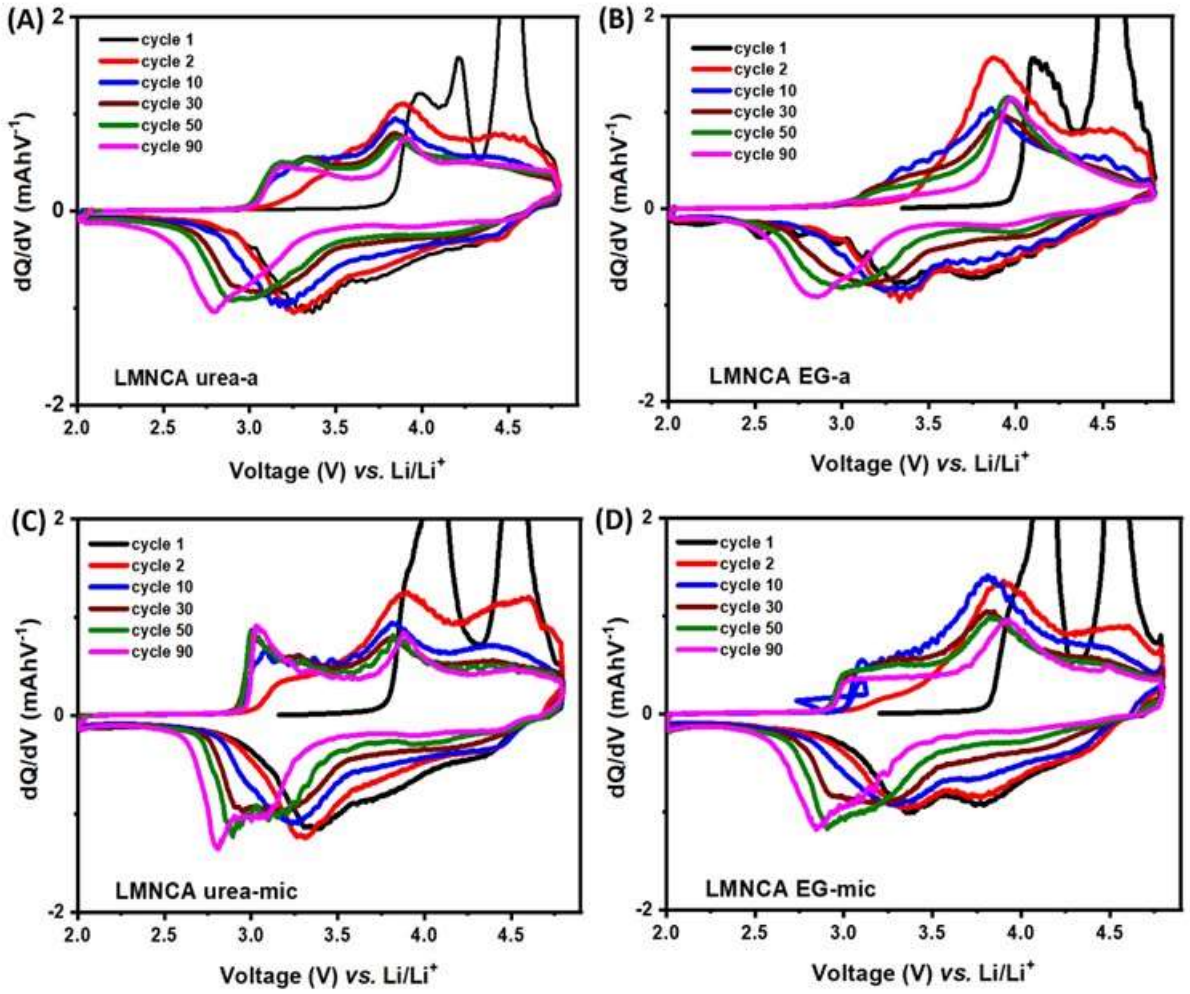

Figure 6: Differential capacity curves (dQ/dV *vs*. V) at 0.1 C measured between 2.0 – 4.8 V *vs*. Li/Li^+ for LMNCA urea-a (A), LMNCA EG-a (B), LMNCA urea-mic (C) and LMNCA EG-mic (D) samples.

Accepted Manuscript

This article is protected by copyright. All rights reserved.

3.6 Electrochemical Impedance Spectroscopy

Figure 7(a, c) shows the Nyquist plots (-Z'' vs. Z') obtained from the electrochemical impedance spectroscopy analysis and fitted with the equivalent circuit shown in Figure 7a inset. The fitting parameters involved: the solution resistance of the electrode system (R_s) due to resistance of the electrolyte and intrinsic cell resistance; the surface film resistance (R_f) and constant phase element (CPE_f), referring to the resistance and capacitance due to the solid-electrolyte interphase (SEI) layer formed on the electrode surface; the charge transfer resistance (R_{ct}) and capacitance (CPE_{Li}), corresponding to charge transfer at the interface between the electrode and the electrolyte, and the Warburg element (Z_w) describing the solid-state diffusion of Li-ion between the particles of active materials and electrolyte, signified by the straight sloping line (~45°) at the low frequency region. Table 3 summarises the EIS results measured at OCV before and after cycling, and the fitted EIS data is shown in Table S1. R_{ct} and R_s values for all the samples increases after 90 cycles as expected due to the effects of electrolyte decomposition and SEI formation upon cycling. However, low impedance is observed for LMNCA urea-mic and LMNCA EG-mic compared to their non-microwave irradiated derivatives LMNCA urea-a and LMNCA EG-a for fresh cells. These results coincide with the improved cycle performance and rate capability in both LMNCA urea-mic and LMNCA EG-mic. Smaller particles result in high area for electrode reaction and thus shortened lithium diffusion path. This facilitate the charge transfer process and lithium diffusion in LMNCA urea-mic and LMNCA EG-mic. LMNCA urea-mic show higher impedance after 90 cycles compared to the other samples as a consequence of more Li_2MnO_3 activation exhibited by LMNCA urea-mic which results in extensive removal of Li_2O causing damage of the electrode surface and thus increase the cell impedance. The post-mortem EDX and XPS analyses of electrodes after cycling (Figure S5) suggest more surface decomposition in urea based LMNCA cathode. The observed compound on the electrode surface is due to the insoluble $Li_xPF_yO_z$, Li_3PO_4 and LiF precipitates due to the decomposition of electrolyte.

Figure 7 (c, d) show Z' *vs.* $\omega^{-1/2}$ curves before and after cycling and the calculated Li-ion diffusion coefficient (D_{Li}^+) values are shown in Table 3. The Li-ion diffusion coefficient values for all the samples are comparable to previously reported values for the LMR-NMC [45]. Similar lithium-ion diffusion kinetics exhibited by LMNCA EG-a and LMNCA EG-mic after 90 cycles are consistent with the sluggish Mn^{3+}/Mn^{4+} redox observed in their dQ/dV studies. The higher lithium diffusion coefficients are obtained for LMNCA urea-mic are due to the

This article is protected by copyright. All rights reserved.

Accepted Manuscript

improved Li-ion diffusion kinetics attributed to increased lattice parameter, further reduction of Mn^{4+} content and small particle sizes.

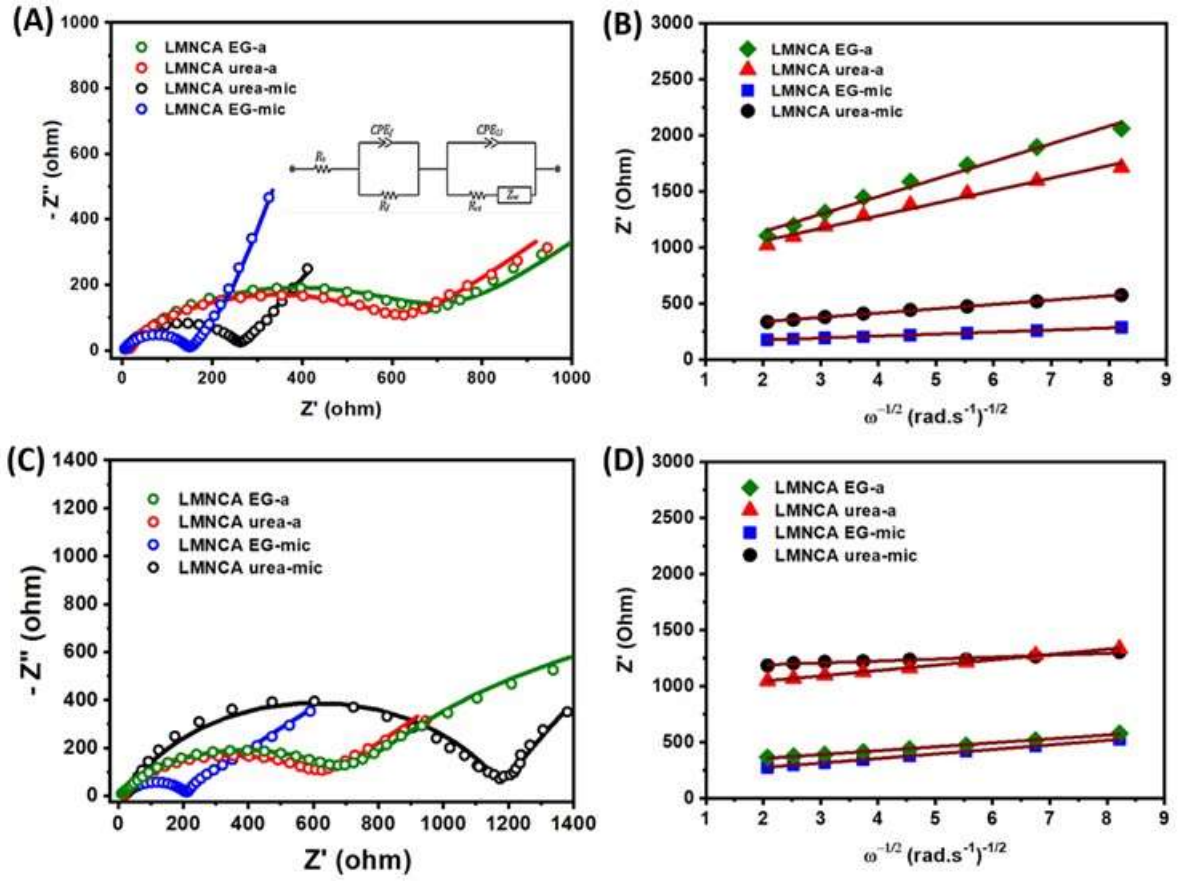

Figure 7: (a) Nyquist plots (-*Z*″ *vs.* *Z*′) of fresh cells and (b) *Z*′ *vs.* $\omega^{-1/2}$ curves of fresh cells, (c) Nyquist plots (-*Z*″ *vs.* *Z*′) after 90 cycles, and (d) *Z*′ *vs.* $\omega^{-1/2}$ curves after 90 cycles for LMNCA urea-a, LMNCA EG-a, LMNCA urea-mic and LMNCA EG-mic samples.

Accepted Manuscript

This article is protected by copyright. All rights reserved.

10.1002/elan.202060373

Table 3: Fitted electrochemical impedance spectroscopy parameters and Li-ion diffusion coefficient values

Electrode material	Electrode condition	**R_{SEI} (Ω)**	**R_f (Ω)**	**R_{CT} (Ω)**	**Z ($\Omega\ s^{-1/2}$)**	**D_{Li+} (cm^2s^{-1}) x10^{-14}**
LMNCA EG-a	Fresh	3.2	65.6	719.9	216.0	0.78
	90^{th} cycle	10.1	96.6	775.9	76.0	1.22
LMNCA urea-a	Fresh	13.6	57.5	544.0	322.0	0.28
	90^{th} cycle	16.7	112.2	806.4	152.0	1.86
LMNCA EG-mic	Fresh	3.9	24.0	142.2	138.2	0.55
	90^{th} cycle	17.3	37.3	142.8	86.8	1.18
LMNCA urea-mic	Fresh	2.7	138.0	157.1	94.2	1.36
	90^{th} cycle	20.1	228.0	971.0	119.2	6.66

Accepted Manuscript

This article is protected by copyright. All rights reserved.

4. Conclusions

The hybrid microwave irradiation-combustion synthesis is shown to be effective for the synthesis of LMR-NMC oxides with improved electrochemical performance. The SEM analysis shows that the morphology of the powders can be tuned by different fuels. However, the hybrid microwave irradiation-combustion method resulted in smaller particles with better particle distribution for LMNCA urea-mic and LMNCA-EG-mic. Additionally, the microwave irradiation resulted in the reduction of transition metal (Mn and Ni) oxidation state and creation of more oxygen vacancies. Out of all the samples, LMNCA urea-mic exhibited enhanced specific capacity, capacity retention and rate capability. The improved cycle performance and rate capability in LMNCA urea-mic are mainly due to the reduced particle sizes, enhanced electronic conductivity due to formation of more oxygen vacancies and reduction of Mn^{4+} ions content and higher Li-ion diffusion coefficient.

Acknowledgements

The authors sincerely appreciate the financial support from the University of the Witwatersrand (Wits), the Council for Scientific and Industrial Research (CSIR) and the Nation Research Foundation (NRF, Grant No: 113638).

Conflict of interest

Authors declare no conflict of interest.

Data availability statement

The data supporting the findings of this study are available in the supporting information file of this article.

Accepted Manuscript

This article is protected by copyright. All rights reserved.

References

[1] M.M. Thackeray, S.H. Kang, C.S. Johnson, J.T. Vaughey, R. Benedek, S.A. Hackney, J. Mater. Chem. 17, **2007**, 3112–3125.

[2] J. Wang, X. He, E. Paillard, N. Laszczynski, J. Li, S. Passerini, Adv. Energy Mater. 6, **2016**, 1600906.

[3] H. Yu, H. Zhou, J. Phys. Chem. Lett. 4, **2013**, 1268–1280.

[4] M.M. Thackeray, S.H. Kang, C.S. Johnson, J.T. Vaughey, S.A. Hackney, Electrochem. Commun. 8, **2006**, 1531–1538.

[5] Z. Lu, L.Y. Beaulieu, R.A. Donaberger, C.L. Thomas, J.R. Dahn, J. Electrochem. Soc. 149, **2002**, A778.

[6] D. Mohanty, A. Huq, E.A. Payzant, A.S. Sefat, J. Li, D.P. Abraham, D.L. Wood, C. Daniel, Chem. Mater. 25, **2013**, 4064–4070.

[7] G. Assat, D. Foix, C. Delacourt, A. Iadecola, R. Dedryvère, J.M. Tarascon, Nat. Commun. 8, **2017**, 1-12.

[8] S. Muhammad, H. Kim, Y. Kim, D. Kim, J.H. Song, J. Yoon, J.H. Park, S.J. Ahn, S.H. Kang, M.M. Thackeray, Nano Energy. 21, **2016**, 172–184.

[9] A.R. Armstrong, M. Holzapfel, P. Novák, C.S. Johnson, S.H. Kang, M.M. Thackeray, P.G. Bruce, J. Am. Chem. Soc. 128, **2006**, 8694–8698.

[10] G. Assat, J.M. Tarascon, Nat. Energy. 3, **2018**, 373–386.

[11] K. Luo, M.R. Roberts, R. Hao, N. Guerrini, D.M. Pickup, Y.S. Liu, K. Edström, J. Guo, A. v. Chadwick, L.C. Duda, P.G. Bruce, Nat. Chem. 8, **2016**, 684–691.

[12] A. Ito, D. Li, Y. Sato, M. Arao, M. Watanabe, M. Hatano, H. Horie, Y. Ohsawa, J. Power Sources. 195, **2010**, 567–573.

[13] J. Zheng, W. Shi, M. Gu, J. Xiao, P. Zuo, C. Wang, J.-G. Zhang, J. Electrochem. Soc. 160, **2013**, A2212–A2219.

[14] S.K. Martha, J. Nanda, G.M. Veith, N.J. Dudney, J. Power Sources. 199, **2012**, 220–226.

Accepted Manuscript

This article is protected by copyright. All rights reserved.

[15] N. Yabuuchi, K. Yoshii, S.T. Myung, I. Nakai, S. Komaba, J. Am. Chem. Soc. 133, **2011**, 4404–4419.

[16] S. Guo, H. Yu, P. Liu, X. Liu, D. Li, M. Chen, M. Ishida, H. Zhou, J. Mater. Chem.A. 2, **2014**, 4422–4428.

[17] H.Z. Zhang, Q.Q. Qiao, G.R. Li, S.H. Ye, X.P. Gao, J. Mater. Chem. 22, **2012**, 13104–13109.

[18] X. Yu, Y. Lyu, L. Gu, H. Wu, S.M. Bak, Y. Zhou, K. Amine, S.N. Ehrlich, H. Li, K.W. Nam, X.Q. Yang, Adv. Energy Mater. 4, **2014**, 1–11.

[19] K. Kang, G. Ceder, Phys. Rev. B Condens. Matter. 74, **2006**, 1–7.

[20] M. Gu, I. Belharouak, J. Zheng, H. Wu, J. Xiao, A. Genc, K. Amine, S. Thevuthasan, D.R. Baer, J.G. Zhang, N.D. Browning, J. Liu, C. Wang, ACS Nano. 7, **2013**, 760–767.

[21] A. Ito, K. Shoda, Y. Sato, M. Hatano, H. Horie, Y. Ohsawa, J. Power Sources. 196, **2011**, 4785–4790.

[22] T. Tang, H.L. Zhang, Electrochim. Acta. 191, **2016**, 263–269.

[23] B. Song, M.O. Lai, L. Lu, Electrochim. Acta. 80, **2012**, 187–195.

[24] Z. Huang, X. Li, Y. Liang, Z. He, H. Chen, Z. Wang, H. Guo, Solid State Ion. 282, **2015**, 88–94.

[25] R. Yu, Y. Lin, Z. Huang, Electrochim. Acta. 173, **2015**, 515–522.

[26] Z. Wang, E. Liu, C. He, C. Shi, J. Li, N. Zhao, J. Power Sources. 236, **2013**, 25–32.

[27] N. Leifer, T. Penki, R. Nanda, J. Grinblat, S. Luski, D. Aurbach, G. Goobes, Phys. Chem. Chem. Phys. 22, 2020, 9098–9109.

[28] J.M. Zheng, X.B. Wu, Y. Yang, Electrochim. Acta. 56, **2011**, 3071–3078.

[29] F.T. Li, J. Ran, M. Jaroniec, S.Z. Qiao, Nanoscale. 7, **2015**, 17590–17610.

[30] S.T. Aruna, A.S. Mukasyan, Curr. Opin. Solid State Mater. Sci.12, **2008**, 44–50.

[31] C.J. Jafta, K. Raju, M.K. Mathe, N. Manyala, K.I. Ozoemena, J. Electrochem. Soc. 162, **2015**, A768–A773.

Accepted Manuscript

This article is protected by copyright. All rights reserved.

[32] F.P. Nkosi, K. Raju, N. Palaniyandy, M. V. Reddy, C. Billing, K.I. Ozoemena, J. Electrochem. Soc. 164, **2017**, A3362–A3370.

[33] K. Raju, F.P. Nkosi, E. Viswanathan, M.K. Mathe, K. Damodaran, K.I. Ozoemena, Phys. Chem. Chem. Phys. 18, **2016**, 13074–13083.

[34] F.P. Nkosi, C.J. Jafta, M. Kebede, L. le Roux, M.K. Mathe, K.I. Ozoemena, RSC Adv. 5, **2015**, 32256–32262.

[35] M. Lou, H. Zhong, H.T. Yu, S.S. Fan, Y. Xie, T.F. Yi, Electrochim. Acta. 237, **2017**, 217–226.

[36] X. Zhang, D. Luo, G. Li, J. Zheng, C. Yu, X. Guan, C. Fu, X. Huang, L. Li, J. Mater. Chem. A. 1, **2013**, 9721–9729.

[37] Q. Li, D. Ning, D. Zhou, K. An, D. Wong, L. Zhang, Z. Chen, G. Schuck, C. Schulz, Z. Xu, G. Schumacher, X. Liu, J. Mater. Chem. A. 8, **2020**, 7733–7745.

[38] T. Nakamura, H. Gao, K. Ohta, Y. Kimura, Y. Tamenori, K. Nitta, T. Ina, M. Oishi, K. Amezawa, J. Mater. Chem.A. 7, **2019**, 5009–5019.

[39] T. Nakamura, Y. Ling, K. Amezawa, J. Mater. Chem. A. 3, **2015**, 10471–10479.

[40] D. Marrocchelli, S.R. Bishop, H.L. Tuller, B. Yildiz, Adv. Funct. Mater. 22, **2012**, 1958–1965.

[41] G. Sun, X. Yin, W. Yang, A. Song, C. Jia, W. Yang, Q. Du, Z. Ma, G. Shao, Phys. Chem. Chem. Phys. 19, **2017**, 29886–29894.

[42] P. Reale, D. Privitera, S. Panero, B. Scrosati, Solid State Ion. 178, **2007**, 1390–1397.

[43] T. Zhang, J.T. Li, J. Liu, Y.P. Deng, Z.G. Wu, Z.W. Yin, J.H. Wu, L. Huang, S.G. Sun, ChemElectroChem. 3, **2016**, 98–104.

[44] R.E. Ruther, A.F. Callender, H. Zhou, S.K. Martha, J. Nanda, J. Electrochem. Soc. 162, **2015**, A98–A102.

[45] C. Fu, G. Li, D. Luo, J. Zheng, L. Li, J. Mater. Chem. A. 2, **2014**,1471–1483.

[46] K.R. Prakasha, M. Sathish, P. Bera, A.S. Prakash, ACS Omega. 2, **2017**, 2308–2316.

Accepted Manuscript

This article is protected by copyright. All rights reserved.

[47] B. Qiu, M. Zhang, L. Wu, J. Wang, Y. Xia, D. Qian, H. Liu, S. Hy, Y. Chen, K. An, Y. Zhu, Z. Liu, Y.S. Meng, Nat. Commun. 7, **2016**, 1–10.

[48] S. Jain, J. Shah, N.S. Negi, C. Sharma, R.K. Kotnala, International Journal of Energy Research. 43, **2019**, 4743–4755.

[49] Z.A. Elsiddig, H. Xu, D. Wang, W. Zhang, X. Guo, Y. Zhang, Z. Sun, J. Chen, Electrochim. Acta. 253, **2017**, 422–429.

[50] C.J. Jafta, K.I. Ozoemena, M.K. Mathe, W.D. Roos, Electrochim. Acta. 85, **2012**, 411–422.

Figure Legends

Figure 1: Hybrid microwave irradiation-combustion synthesis of LMNCA powders.

Figure 2: SEM images of LMNCA urea-a, LMNCA EG-a, LMNCA urea-mic and LMNCA EG-mic samples.

Figure 3: (a) XRD patterns and (b) Raman spectra of LMNCA urea-a, LMNCA EG-a, LMNCA urea-mic and LMNCA EG-mic samples.

Figure 4: XPS data of (a) Co $2p_{3/2}$, (b)Ni $2p_{3/2}$, (c) Mn $2p_{3/2}$ and (d) O 1s for of LMNCA urea-a, LMNCA EG-a, LMNCA urea-mic and LMNCA EG-mic samples.

Figure 5: (a) Cyclic voltammetry at 0.1 mV s^{-1} (b) Galvanostatic charge-discharge 1^{st} cycles at 0.1 C (c) Cycle performance at 0.1 C measured (d) Cycle performance at 2C, and (e) Rate capability at 0.5, 1, 2, and 5 C for LMNCA urea-a, LMNCA EG-a, LMNCA urea-mic and LMNCA EG-mic samples. All studies were measured between 2.0 – 4.8 V vs. Li/Li^+.

Figure 6: Differential capacity curves (dQ/dV *vs.* V) at 0.1 C measured between 2.0 – 4.8 V *vs.* Li/Li^+ for LMNCA urea-a (A), LMNCA EG-a (B), LMNCA urea-mic (C) and LMNCA EG-mic (D) samples.

Figure 7: (a) Nyquist plots (-Z″ *vs.* Z′) of fresh cells and (b) Z′ *vs.* $\omega^{-1/2}$ curves of fresh cells, (c) Nyquist plots (-Z″ vs. Z′) after 90 cycles, and (d) Z′ *vs.* $\omega^{-1/2}$ curves after 90 cycles for LMNCA urea-a, LMNCA EG-a, LMNCA urea-mic and LMNCA EG-mic samples.

This article is protected by copyright. All rights reserved.

Accepted Manuscript